Journal of Non-Crystalline Solids 121 (1990) 294–302
North-Holland

Section 4. Physical and chemical properties of shaped materials: (c) Thin films and coating

SOL–GEL THIN FILM FORMATION

C.J. BRINKER, A.J. HURD, G.C. FRYE, K.J. WARD and C.S. ASHLEY

Division 1846, Sandia National Laboratories, Albuquerque, NM 87185-5800, USA

The overlap between the drying stage and the aggregation/gelation and aging stages of sol–gel film formation establishes a brief time for further condensation reactions to occur. For this reason, the structures of films are often considerably more compact than those of the corresponding bulk gels or xerogels prepared from identical precursors. Experimental techniques to study film formation and the structure of the deposited film in situ have been developed. These techniques include imaging ellipsometry, infrared microscopy and gas sorption on surface acoustic wave substrates.

1. Introduction

During sol–gel thin film formation via dipping, inorganic or metal organic sols are deposited on the substrate surface by a complex steady-state process * combining gravitational draining, solvent evaporation, and continued condensation reactions [1,2] (see fig. 1). Unlike conventional bulk gel formation, the drying stage overlaps the aggregation/gelation and aging stages, establishing only a brief time span for condensation reactions to occur [3]. In addition, the entrainment of the inorganic species in the draining fluid layer establishes a shear field that increases with substrate withdrawal speed U_0. The structure of the final deposited film depends on the competition between such phenomena as evaporation (which compacts the film), condensation reactions (which strengthen the film, increasing its resistance to compaction) and shear-induced ordering [2]. Often, compared with bulk gels, the brief time span of the deposition process causes the film structure to remain more compliant, allowing it to collapse at the final stage of drying as the liquid–vapor menisci recede into the film interior [1,2].

Owing to the differences between bulk and thin film gel formation, studies of bulk gels are generally inappropriate for deriving structural information pertinent to thin films. However, due to the time scale of the deposition process and the thickness of the final deposited layer (generally $\ll 1$ μm), there have been rather few investigations attempting to obtain structural information directly from the depositing or dried film itself. This brief paper summarizes results of recent in situ investigations of sol–gel film formation utilizing the following techniques: (1) conventional and broad beam (imaging) ellipsometry; (2) FTIR microscopy; and (3) gas sorption on surface acoustic wave (SAW) substrates.

2. Ellipsometry

Draining and evaporation accompanying dipping (fig. 1) cause the thickness h and volume fraction solids ϕ of the depositing film to change continuously with distance above the reservoir surface. For a constant withdrawal speed U_0 and controlled ventilation, steady-state h and ϕ profiles are established. According to gravitational draining theory with negligible surface tension or evaporation, the thickness of the entrained fluid near the reservoir surface approaches $\lambda = (\eta U_0/\rho g)^{1/2}$ [4] (see fig. 1). With volatile solvents, the shape of the profile and distance X_0 from reservoir to drying line depends on the competition between draining and evaporation. For gravitational draining with a constant evaporation rate

* The dip-coating process is steady-state with respect to the reservoir surface.

0022-3093/90/$03.50

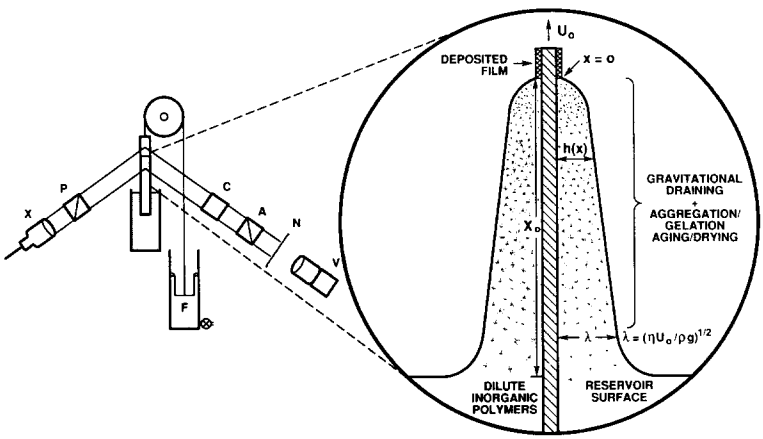

Fig. 1. Schematic of the dip-coating apparatus, ellipsometer and steady-state, sol–gel film forming process. Concurrent draining and evaporation cause solution precursors to be concentrated on the substrate surface. Continued evaporation of solvent leads to the formation of porosity during the latter stages of film formation. Refractive index and thickness profiles of the complete film forming process are measured using the ellipsometer. It consists of a beam expander X, polarizer P, quarter-wave compensator C, analyzing polarizer A, diffusing screen N, and video camera V.

E, Hurd [5] has shown that the thickness profile is a wedge shape governed by

$$Sx = h\left(1 - h^2/3\lambda^2\right), \tag{1}$$

where S, a 'dynamic contact angle' at the apex of the wedge, equals $E/\rho U_0$ and $h(x)$ is the film thickness as a function of position x from the drying line. This equation, plotted in fig. 2, predicts a wedge profile with $S = 10^{-3}$ rad for $E = 10^{-5}$ g s^{-1} cm^{-2} and height (from the reservoir) of the drying front $X_0 = 2\lambda/3S \approx 1$ cm. Steady-state conditions and the fact that all fluid elements are moving upward (no circulating backflow) * require that the solids mass in any horizontal slice must be constant [5],

$$h(x)\phi(x) = \text{constant}, \tag{2}$$

so ϕ varies inversely with h in the thinning film.

To measure the h, ϕ profile of the entrained fluid film from reservoir to drying line in situ, and thus test the predictions of the model, Hurd and Brinker developed a broad beam (imaging) ellipsometer [5,6]. Ellipsometry depends on changes in amplitudes and phases of components of the incident light polarized parallel and perpendicular to the substrate surface when reflected. The imaging ellipsometer consists of a beam expander, polarizer, substrate, compensator plate, analyzing polarizer and detector (fig. 1). The angle of the polarizer determines the relative amplitudes of the incident s and p waves. The amplitude of the reflected s and p waves are determined by their respective reflection coefficients, R_s and R_p. The polarizer and analyzer angles A and P are the adjustable parameters used to determine the refractive index and thickness of the film via these complex reflection coefficients using various detection schemes. By illuminating the depositing film with a broad collimated beam, every ray in the beam can be used to ellipsometrically image

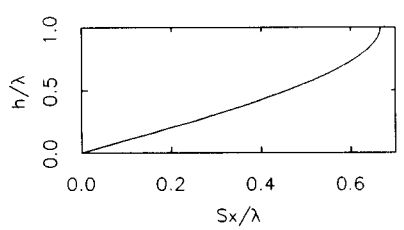

Fig. 2. Thickness profile assuming constant evaporation and no curvature effects.

* For our conditions backflow occurs mainly within the reservoir and the stagnation point is near the reservoir surface.

the spatially varying thickness and index over the entire substrate surface [5,6].

Figure 3 shows a typical sequence of ellipsometric images of a titania film during deposition from a metal organic sol in ethanol. The frames were recorded with different analyzer angles (to ensure that a null condition was achieved somewhere within the image), accounting for the different positions and intensities of fringes within the steady state drying film. Figures 4(a) and (c) show

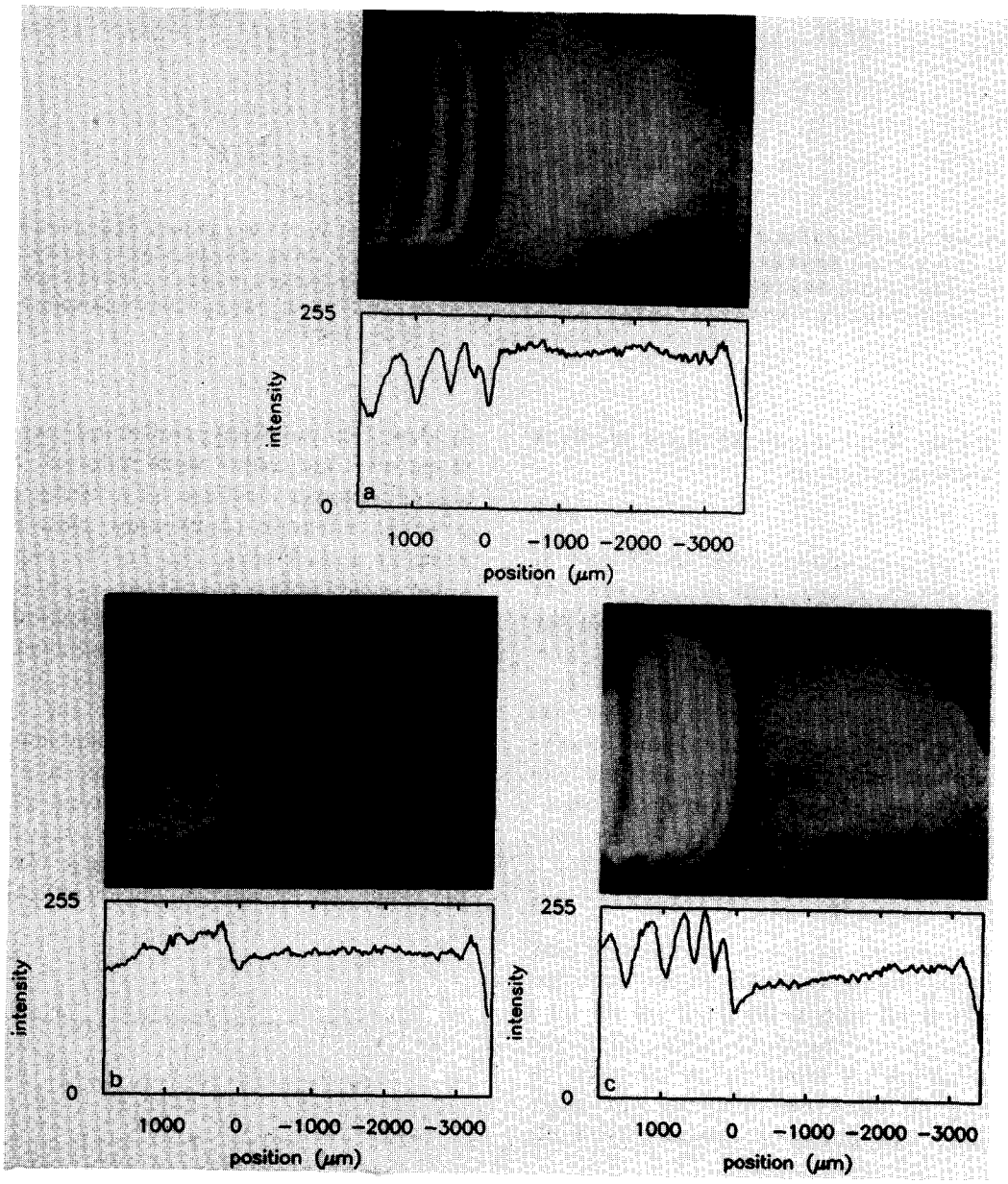

Fig. 3. Ellipsometric images of drying films with different analyzer positions. (a) The fringes correspond to optical thickness fringes of integer multiples of $\lambda/2$; (b) no extinctions are possible and none are seen; (c) the first fringe is passing through a minimum allowing the thickness and refractive index to be calculated along that contour.

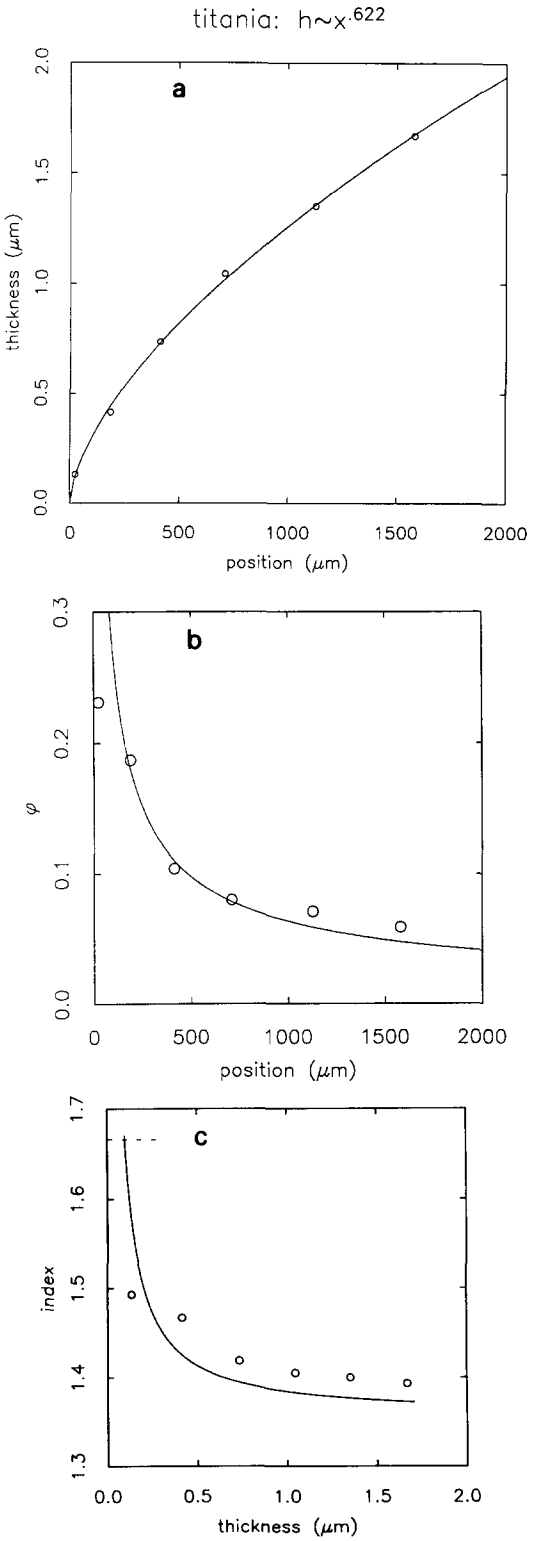

the corresponding thickness and refractive index values derived from a sequence of images. Figure 4(b) shows the profile of ϕ calculated from the refractive index according to the effective medium model by Maxwell Garnet. Comparing figs. 2 and 4(a), a discrepancy is apparent between the constant evaporation model and the actual shape of the film profile in the vicinity of the drying front (x or position $\rightarrow 0$). Whereas eq. (1) predicts a wedge-shaped profile, the thickness profile of the depositing titania sol is distinctly blunt at the drying line.

Since the thickness profiles of pure alcohols are also blunt, the discrepancy between the prediction of the constant evaporation model and the actual fluid profile cannot be explained by the entrained inorganic phase. By analogy to the electric field singularity at the tip of a lightning rod [7], Hurd developed a ventilation-limited evaporation model in which solvent vapor transport and attending evaporation rate are greater near the drying line, resulting in a parabolic thickness profile:

$$h(x)\left(1 - h(x)^2/3\lambda^2\right) \underset{x\rightarrow 0}{=} Sx^{1/2}. \tag{3}$$

Ellipsometric imaging of a variety of pure solvents as well as various weakly branched and particulate titania and silica sols showed reasonably good agreement with the $h(x) \sim x^{1/2}$ prediction, as illustrated in fig. 4(a) where $h(x) \sim x^{0.622}$. (The slightly higher exponent may be due to the fact that the film is 3-dimensional, not 2-dimensional as assumed in eq. (3).) For inorganic sol deposition, this suggests that the thickness profile is relatively unaffected by the concentrating sol, so

Fig. 4. (a) Thickness profile of drying titanate film. The displacement along the film was measured from a fudicial near the drying front. The solid line represents the prediction from gravitational draining with non-constant evaporation model ($h \sim x^{0.622}$). (b) Profile of volume fraction solids of the drying titanate film. Solid line is $\phi \sim x^{-0.622}$. (c) Index–thickness curve of the drying titanate film. Solid line is theoretical curve for the assumed condition $h(x)\phi(x) =$ constant, where ϕ is related to n according to the Maxwell Garnet model. Dashed line is the refractive index of the fully dried film, 1.67.

that ϕ should vary as $1/h \sim x^{-1/2}$. The ϕ profiles determined for a number of titania and silica sols (see fig. 4(b)) generally showed $\phi \sim x^{-1/2}$ behavior except in close proximity to the drying line where there is a slowing down of the increase in ϕ for $\phi > 0.2$ followed by a dramatic increase in ϕ in the final dried film [5,6]. The slowing down may be evidence for either a kinetically limited approach to concentrated states (e g., due to the viscosity divergence associated with the percolation threshold) or the formation of a 'skin'. The dramatic increase in ϕ and n very near the drying line (fig. 4(c)) is attributed to the collapse of the sol network within a narrow region of x due to the capillary pressure exerted by liquid–vapor menisci as they recede into the film interior [1,2]. The extent of this collapse is greatest for weakly branched precursors deposited under conditions where little further condensation occurs. Conversely, for sols composed of aggregated particulate precursors, final drying occurs with little collapse of the sol network, because the capillary pressure ($\propto 1/$pore size) is much less and the stiffness of the network is much greater. In this case a long-lived partially wetted state is observed near the drying line [6].

Deviation from the expected $h \sim x^{1/2}$ behavior was also observed for alcohol–water mixtures containing greater than 10 vol.% water. A water rich region becomes concentrated at the drying line and grows with time without reaching steady state within the duration of the dipping experiment (~ 1 min). Since water is a component of many inorganic sols, concentrations of water in excess of the azeotropic composition may influence the film profile in the vicinity of the drying line. In addition, conducting the final stage of drying in a water rich environment may cause greater film collapse due to the higher surface tension of water. Consistent with this idea, Glaser and Pantano [8] observed that the density of as-deposited silicate films increased with the quantity of water added in excess of that required for complete hydrolysis of tetraethoxysilane ($H_2O/Si = 4$–40). This trend is just the opposite of that observed in bulk silica gels (density decreases with H_2O/Si [9]) and may be explained by water enrichment near the drying line.

3. Infrared microscopy

Chemical information such as the extent of condensation or evaporation may be derived from the steady-state dipping profile utilizing spatially resolved spectroscopic techniques such as Fourier transform infrared (FTIR) microscopy [10]. In this method an IR beam is focused on the film surface with 100 μm resolution in the x direction. A portion of the beam is reflected from the film surface. The remainder of the beam passes into the film and may be reflected from the substrate surface, passing through the film a second time. For total pathlengths less than about 10 μm, the beam emerges from the film and is collected with the microscope optics along with the reflectance signal, producing a reflection–absorption spectrum. For thicker films, the beam is totally absorbed within the film and only the reflectance signal is collected by the infrared detector. For very thin films, the contribution of the reflectance component dominates the spectrum, since the short pathlength through the film results in little infrared absorption.

Since the pathlength depends on the thickness of the film and hence the distance above the reservoir surface, the IR spectra may vary from pure reflection (thick films: transmitted beam completely absorbed) to reflection–absorption to primarily reflection (very thin films: transmitted beam shows minimal absorption) as $h \to 0$. Spectral changes due to the different contributions of reflection and absorption are evident in the infrared microspectroscopy data shown in fig. 5 as a function of film thickness. These spectra were constructed by coaddition of a pure specular reflectance spectrum obtained from a deep pool of the sample and a percentage of a 15 μm transmission spectrum of the fluid to adjust the transmission pathlengths. Ethanol spectra (fig. 5(a)) are representative of a liquid continuously thinned by evaporation and draining. For the case of a depositing sol, both the pathlength and composition vary continuously with x as the inorganic component becomes concentrated in the thinning film. Fig. 5(b) shows spectral simulations for TEOS concentrated in a thinning ethanol solvent. Comparison with experiment requires subtraction of

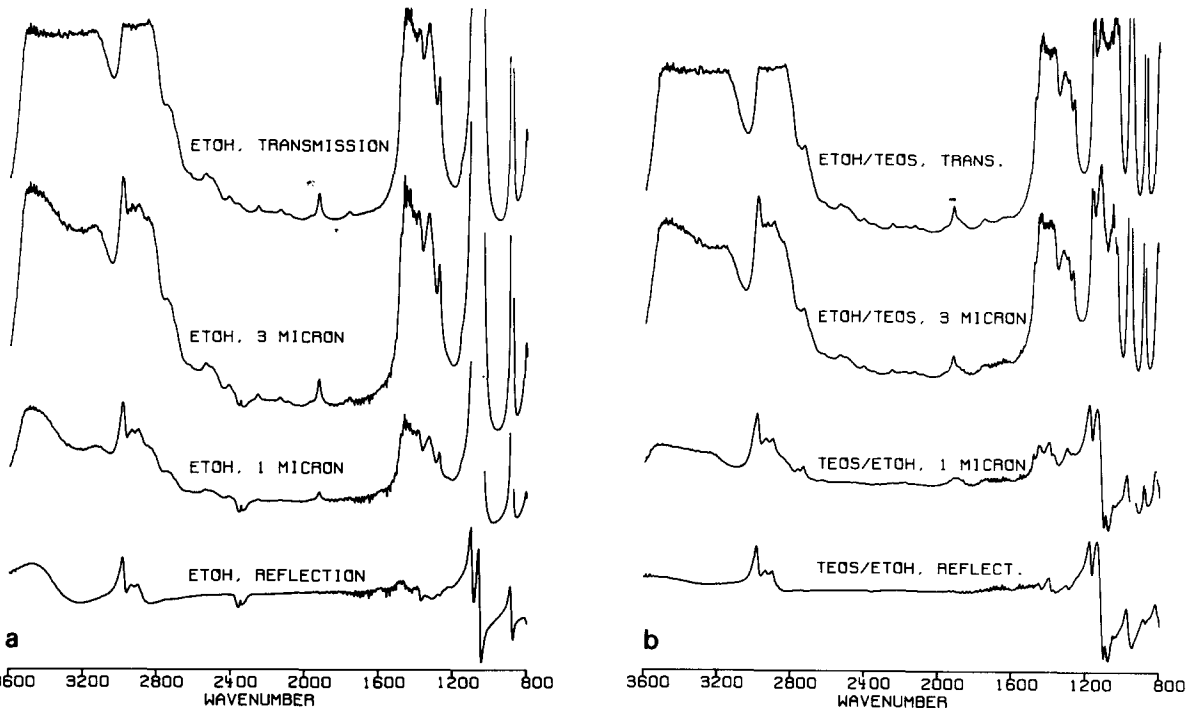

Fig. 5. (a). Simulated FTIR spectra of a thinning ethanol film during draining and evaporation compared to the transmission spectrum of ethanol (top) and reflection spectrum (bottom). (b) Simulated spectra of TEOS concentrated in a thinning ethanol film during draining and evaporation compared to a transmission spectrum of 5:2 (vol) EtOH:TEOS (top) and a reflection spectrum of 2:5 (vol) EtOH:TEOS (bottom). The 3 μm spectrum consists of 5:2 (vol) EtOH:TEOS. The 1 μm film consists of 2:5 (vol) EtOH:TEOS.

the alcohol vapor solvent and an independent measure of pathlength. (We are currently reconfiguring the microscope optics to perform simultaneous interferometry to determine the pathlength.)

4. Gas sorption on SAW substrates

As discussed in the introduction, the evaporation rate establishes a brief timespan for the aggregation/gelation, aging and drying stages of the film deposition process. The final film structure depends largely on the precursor structure (weakly branched, strongly branched, particulate) and its response to rapid concentration resulting first from solvent evaporation and then from the attending capillary pressure as liquid–vapor menisci recede into the film interior. In general, due to the brief duration of the deposition process, films are less highly condensed than bulk gels and collapse to a greater extent on drying. For this reason, the structure of a dried film (e.g., pore volume, pore size, surface area) often differs from its bulk xerogel counterpart, requiring that structural studies be conducted on the film itself.

Due to the low total pore volumes present in typical sol–gel derived films 100–300 nm thick, conventional methods of characterizing porosity/microstructure are not sufficiently sensitive to provide useful information. To overcome this problem, Frye et al. [11] developed a surface acoustic wave (SAW) technique sufficiently sensitive to measure gas adsorption/desorption isotherms on ~1 cm^2 areas of typical sol–gel films. In this technique, a sol–gel film is deposited on the surface of a SAW device composed of two interdigital transducers on the surface of a piezoelectric substrate (see fig. 6). An alternating voltage applied to one transducer launches a surface acoustic wave having a high density of acoustic energy at

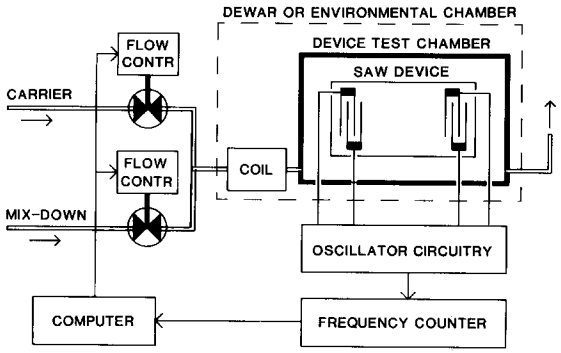

Fig. 6. Schematic of a surface acoustic wave device in the experimental set-up for obtaining nitrogen adsorption–desorption isotherms.

the crystal/film surface. The wave is received by the second transducer. Its velocity is very sensitive to changes in mass or elastic moduli of the film through which it propagates. By incorporating the SAW device as the frequency control element in an oscillator circuit, changes in the wave velocity are manifested as changes in the circuit frequency.

SAW devices may be used to measure physical adsorption by the film as in a typical N_2 sorption experiment (see fig. 6). When the frequency response results only from mass loading, frequency changes are related to the amount of adsorbed nitrogen by [9]

$$\Delta f/f_0 = \kappa\, \Delta v/v_0 = -\kappa c_m f_0 mn \qquad (4)$$

where κ is the fraction of the path length between transducers covered by the film, c_m is the mass sensitivity of the device, v_0 and f_0 are the unperturbed wave velocity and oscillator frequency, respectively, m is the mass of an N_2 molecule, and n is the number areal density of the adsorbed molecules. For a quartz substrate, the detection limit is 80 pg/cm^2 of film, or 0.003 monolayers of N_2 on a flat SAW substrate. As shown in figs. 7–9, this is sufficient sensitivity to obtain high quality N_2 adsorption–desorption isotherms even on non-porous films.

Figure 7 illustrates the differences in microstructure of films and monolithic gels made from identical silicate precursors (TEOS : EtOH : H_2O : HCl = 1 : 3 : 5.1 : 0.058). The bulk gel isotherm (fig. 7(a)) is of type I, indicative of a microporous solid (pore diameters $\leq$ 2 nm and BET surface area = 850 m^2/g). The film isotherm (fig. 7(b)) is of type II indicative of adsorption on a non-porous surface. The type II isotherm indicates that the film structure collapses on drying to such a degree that it has no surface area (other than the geometric area of the exterior surface) accessible to N_2 (kinetic diameter = 0.396 nm). These differences reflect the brief time span of the film deposition process (several seconds) compared with the long processing time required to prepare a crack-free monolithic xerogel (~ 1 month). During film formation, the weakly branched acid-catalyzed silicate species remain very compliant, facilitating compaction by solvent evaporation and collapse by the exceedingly high capillary pressure (1–2 kbar) [2].

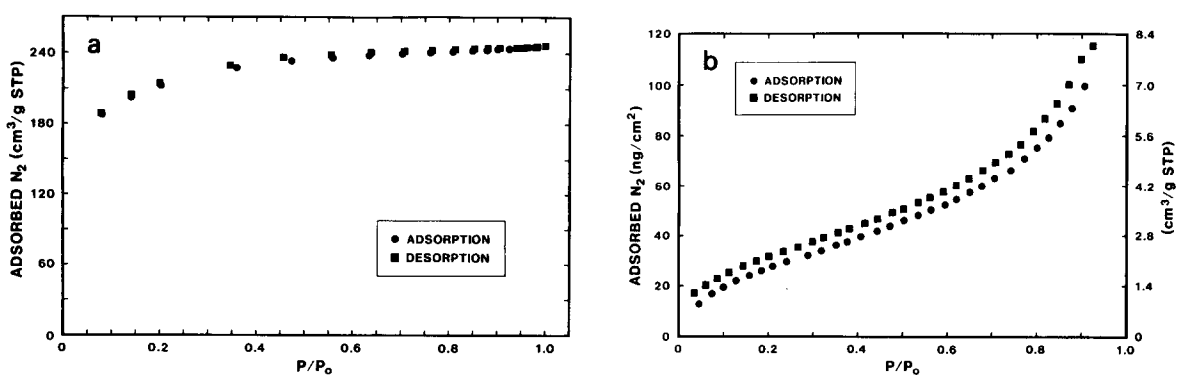

Fig. 7. (a) Type I nitrogen adsorption–desorption isotherm of a bulk silicate xerogel prepared by acid-catalyzed hydrolysis of TEOS followed by slow drying. (b) Type II nitrogen adsorption–desorption isotherm of a film prepared from the same acid-catalyzed silicate precursors as in fig. 7(a). Isotherm was obtained by a SAW device.

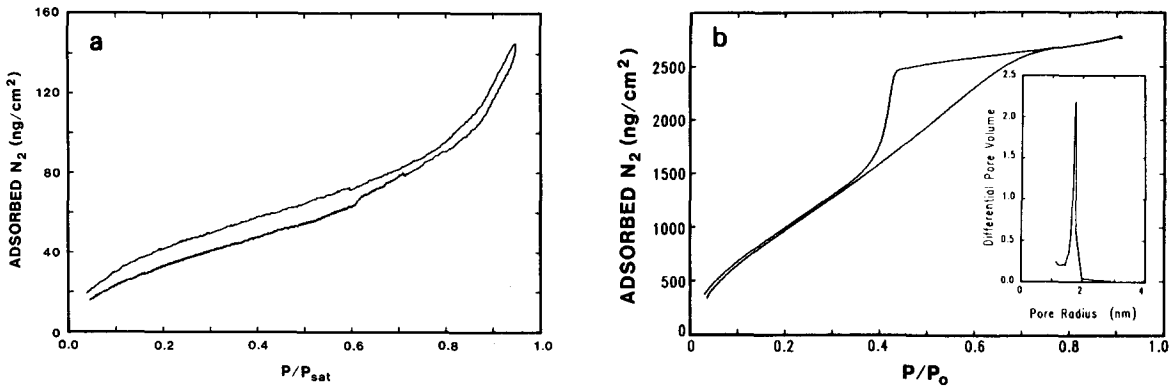

Fig. 8. (a) Type II nitrogen adsorption–desorption isotherm obtained for a multicomponent film prepared from unaged precursors. (b) Type IV nitrogen adsorption–desorption isotherm obtained for a film prepared from precursors aged at 50°C for 1 week prior to deposition. Inset: Pore size distribution obtained from the desorption branch.

Fig. 8 compares SAW N_2 adsorption–desorption isotherms of films prepared from unaged borosilicate precursors and compositionally identical precursors aged one week at 50°C prior to deposition [2]. The film prepared from the unaged precursor is characterized by a type II isotherm (fig. 8(a)), indicating adsorption on a non-porous surface. The isotherm of the film prepared from the aged precursor is of type IV (fig. 8(b)) indicative of adsorption on a mesoporous surface (pore diameters = 2.0–50 nm). One interpretation of the hysteresis is that there are pore cavities larger in diameter than the 'throats' connecting them (so-called ink bottle pores). In the desorption cycle the pressure must be reduced sufficiently to empty the throats before the cavities can empty. Based on this interpretation, the desorption branch can be used to determine the size distribution of the throats as shown in the inset of fig. 8(b). The effect of aging on the pore structure is explained by a fractal aggregation model [2]. Unaged precursors are quite tiny and are compacted by the capillary pressure which is correspondingly high. Aged precursors are much larger and are characterized by a mass fractal dimension, $D = 2.4$. These structures exhibit strong mutual screening

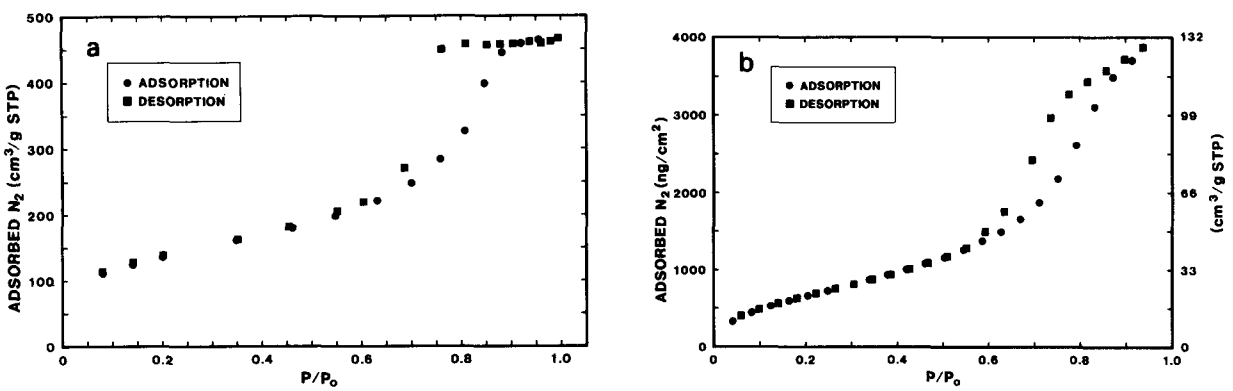

Fig. 9. (a) Type IV nitrogen adsorption–desorption isotherm obtained for a bulk xerogel prepared from repulsive particulate silicate particles. (b) Type IV nitrogen adsorption–desorption isotherm obtained for a film prepared from the same particulate silica particles as in fig. 9(a).

Table 1
Film porosity determined by SAW N_2 sorption for various precursor aging conditions

Sample	Refractive index	Porosity ads. N_2	Median pore radius (nm)	Surface area (m^2/g)
Unaged	1.45	0	< 0.2	1.2–1.9
3 day	1.31	16	1.5	146
1 week	1.25	24	1.6	220
2 week	1.21	33	1.9	263
3 week [a)]	1.18	52	3.0	245

[a)] Sols aged for 3 weeks gelled. They were diluted with ethanol and re-liquified at high shear rates to obtain fluids suitable for coating.

due to the high value of D. Concentration via solvent evaporation causes cluster–cluster aggregation in which the characteristic pore size should scale with the cluster size. During drying the individual clusters are compacted by the capillary pressure, but the aggregated pore structure is preserved, explaining the observed type IV isotherm. Results of pore volume, pore size and surface area measurements as a function of precursor aging times are summarized in table 1 [2].

Figures 9(a) and (b) [11] compare adsorption isotherms for bulk and thin film specimens prepared from identical, spherical silica particles formed by base-catalyzed hydrolysis of TEOS (in this case the bulk gel was prepared by slowly drying the silica sol). Both isotherms are of type IV, varying only in the shape of the desorption branches. Since the sols are essentially completely reacted and the particles mutually repulsive, the different time scales of the film and bulk gel processes are of much less consequence than in the previous example of bulk and thin film microstructures. In both cases, gels are formed by evaporation of the solvent. Further solvent evaporation results in xerogels or films in which porosity is created by the particle packing. The steeper desorption branch observed for the bulk gel does suggest that the longer processing time employed allows the particles to assemble into a more ordered packing geometry with a narrower size distribution of throats.

5. Summary

Sol–gel thin film processing differs from bulk gel processing in that the drying stage overlaps the aggregation/gelation and aging stages establishing a brief time for further condensation reactions or ordering to occur. For these reasons, we have developed in situ methods of characterizing film deposition and the structure of the deposited film. Imaging ellipsometry allows a determination of the spatially varying film thickness and refractive index in the steady-state drying film. FTIR microscopy is potentially useful to obtain spatially resolved chemical information such as the extent of condensation. Sorption experiments on SAW substrates are sufficiently sensitive to obtain adsorption–desorption isotherms even on non-porous films.

References

[1] C.J. Brinker, A.J. Hurd and K.J. Ward, in: Ultrastructure Processing of Advanced Ceramics, eds. J.D. Mackenzie and D.R. Ulrich (Wiley, New York, 1988) p. 223.
[2] C.J. Brinker, G.C. Frye, A.J. Hurd, K.J. Ward and C.S. Ashley, in: Proc. 4th Int. Conf. on Ultrastructure Processing of Glasses, Ceramics and Composites, eds. D.R. Uhlmann and D.R. Ulrich (Wiley, New York, 1990) in press.
[3] L.E. Scriven, in: Better Ceramics Through Chemistry III, eds. C.J. Brinker, D.E. Clark and D.R. Ulrich (Mater. Res. Soc., Pittsburgh, PA, 1988) p. 717.
[4] E.O. Tuck, Phys. Fluids 26 (1983) 2352.
[5] A.J. Hurd and C.J. Brinker, in: Better Ceramics Through Chemistry III, eds. C.J. Brinker, D.E. Clark and D.R. Ulrich (Mater. Res. Soc., Pittsburgh, PA, 1988) p. 731.
[6] A.J. Hurd and C.J. Brinker, J. Phys. (Paris) 49 (1988) 1017.
[7] J.D. Jackson, Classical Electrodynamics, 2nd Ed. (Wiley, New York, 1979) ch. 2.
[8] P.M. Glaser and C.G. Pantano, J. Non-Cryst. Solids 63 (1984) 209.
[9] C.J. Brinker, K.D. Keefer, D.W. Schaefer and C.S. Ashley, J. Non-Cryst. Solids 48 (1982) 47.
[10] R.G. Messerschmidt and M.A. Harthcock, eds., Infrared Microspectrometry (Dekker, New York, 1988).
[11] G.C. Frye, A.J. Ricco, S.J. Martin and C.J. Brinker, in: Better Ceramics Through Chemistry III, eds. C.J. Brinker, D.E. Clark and D.R. Ulrich (Mater. Res. Soc, Pittsburgh, PA, 1988) p. 349.